Microchimica Acta (2021) 188: 410
https://doi.org/10.1007/s00604-021-05063-x

ORIGINAL PAPER

Terthiophene-functionalized mesoporous silica-based fluorescence sensor for the detection of trace methyl orange in aqueous media

Jing Huang[1] · Jing Wang[1,2] · Dong Li[1] · Pengxiang Chen[1] · Hai-Bo Liu[1]

Received: 31 May 2021 / Accepted: 12 October 2021 / Published online: 5 November 2021

Abstract

A terthiophene-functionalized mesoporous SBA-15 silica, i.e., TTU-SBA-15, was successfully developed and used as a highly selective and ultrasensitive fluorescence sensor for methyl orange (MO) detection. When the concentration of MO was increased, the fluorescence emission intensity of TTU-SBA-15 suspensions at 452 nm gradually decreased at an excitation wavelength of 368 nm, and the color of the suspension solutions changed obviously from blue to dark under 365 nm UV light. The fluorescence intensity at 452 nm was linearly proportional to the concentration of MO in the range 0.20 – 2.0 μM, with a detection limit of 0.092 μM. Competitive pollutants, variations in pH, and sample recycling had subtle or negligible effects on the detection of MO. TTU-SBA-15 was applied to the determination of MO in tap water, and recoveries from spiked samples were in the range 98.3 – 103.0%. This study provides a convenient and effective strategy to realize highly sensitive and selective sensors that could target dyes via the functional modification of mesoporous materials.

Keywords Fluorescence sensor · Terthiophene · Methyl orange · Mesoporous silica · SBA-15

Introduction

The inadvertent discharge of organic dyes into aquatic systems causes serious water pollution, which is a great threat to both environmental safety and human health [1–6]. Recent years have witnessed great success in the dye removal technology [7–10], but little attention has been paid to the identification of the dye type and concentration prior to treatment. Therefore, developing simple, fast, and efficient methods for the selective detection of organic dye pollutants, such as methyl orange (MO), even at trace levels in water resources is of great significance.

Currently, several technologies for detecting organic dyes, including capillary surface-enhanced Raman spectroscopy (SERS) [11, 12], high-performance liquid chromatography (HPLC) [13], and liquid chromatography coupled to mass spectrometry (LC–MS) [14], have been developed. Although they are very helpful, HPLC and LC–MS could not be used for rapid detection [15], and SERS is extremely expensive and requires substantial operational skills. Given these issues, fluorescence sensing methods stand out among other approaches because of their simplicity, low cost, high sensitivity, and rapid responses [16–18]. Organic–inorganic hybrid materials show more attractive properties than the organic-based fluorescence sensing systems, particularly in terms of stability and reusability, because these hybrid systems combine the merits of organic and inorganic functional groups. Organic–inorganic hybrid fluorescence materials have been applied for the quantitative detection of organic dyes, such as carbon dots [19], are-earth doped upconversion nanoparticles (UCNPs) [20], nanomicelles [21], etc. while most of the reported fluorescence sensors didn't possess high selectivity and anti-interference ability [15, 22]. For example, Agarwal et al. reported the fluorescence detection of MO, bromophenol, rhodamine 6G, and methylene blue by using N-doped oxidized carbon dots as an optical sensing probe; however, discrimination of these four dyes through the fluorescence response mode was challenging [22]. As such, more effort should be devoted to develop

✉ Jing Wang
wjwyj82@gxu.edu.cn

✉ Hai-Bo Liu
lwllhb@gxu.edu.cn

[1] School of Chemistry and Chemical Engineering, Guangxi University, Nanning 530004, People's Republic of China

[2] Guangxi Key Laboratory of Petrochemical Resource Processing and Process Intensification Technology, Guangxi University, Nanning 530004, People's Republic of China

organic–inorganic hybrid material-based fluorescence sensors that could enable the highly selective and sensitive detection of a target dye, such as MO, in aqueous media.

Organic–inorganic hybrid materials are generally fabricated by immobilizing organic functional units onto an inorganic solid support matrix. Mesoporous silica (e.g., SBA-15 [23]) has attracted considerable attention as an inorganic material on account of its high porosity, large specific surface area, ordered pore channels, and good stability [24–26]. The excellent detection performance of mesoporous silica as an optical sensor would be displayed after the organic functionalization [27–29]; the ideal sensor would consist of the silica material as a solid support and an organic optical receptor or indicator [30, 31]. Reports on functionalized mesoporous silica materials for the detection of various analytes, such as metal ions and anions, bearing various fluorescent reactive receptors are widely available [32–35]. By contrast, studies on fluorescence sensors for organic dyes based on mesoporous silica materials are scarce.

In the present study, we designed an organic–inorganic hybrid mesoporous material-based fluorescence sensor, i.e., TTU-SBA-15, by coupling a terthiophene-based derivative, i.e., TT, and urea-functionalized mesoporous SBA-15 silica. TTU-SBA-15 showed excellent performance for the selective and sensitive detection of trace MO in aqueous media. Specifically, the fluorescence of TTU-SBA-15 was remarkably quenched by addition of MO. A control material, i.e., TT-SBA-15, was also prepared by coupling TT and amine-functionalized mesoporous SBA-15 silica. Compared with this material, TTU-SBA-15 exhibited distinct advantages for MO determination, such as improved selectivity, better anti-interference ability, and higher sensitivity.

Experimental section

Materials

SBA-15 was obtained from Nanjing XFNANO Materials Tech Co., Ltd. (China) and used as received. 2,2′:5′,2″-Terthiophene-5-carbaldehyde (TT), 1-[3-(trimethoxysilyl) propyl]urea (Tpu), 3-(aminopropyl)triethoxysilane (APTES), methyl orange (MO), methyl blue (MB), malachite green (MG), methylene blue (MLB), litmus, 3-amino-7-dimethylaminophenothiazin-5-ium chloride (Azure A), and 3-(dimethyl- amino)-7-(methylamino)phenothiazin-5-ium chloride (Azure B) were purchased from Sigma-Aldrich. Other chemicals and reagents were obtained from commercial suppliers and used without further purification.

Instruments

The small angle X-ray powder diffraction (SXRD) pattern was measured using smartlab9K diffractometer with Cu Kα radiation. Transmission electron microscopy (TEM) images were acquired by using JEOL JEM-2100 F microscope operated at 300 kV. The thermo-gravimetric analysis (TGA) was conducted on a Netzsch STA449-F5 TAQ600 instrument at a heating rate of 10 °C/min. The Fourier transform infrared (FT-IR) spectra were carried out using Varian 660-IR (ATR) FT-IR spectrophotometer. The nitrogen adsorption–desorption isotherms were obtained using a Micrometrics ASAP 2460 instrument. Fluorescence spectra were collected on a 960 MC spectroscopy, with an excitation wavelength of 368 nm, and the slit widths for emission and excitation were 5 and 10 nm, respectively. The fluorescence lifetimes were recorded using Edinburgh FLS1000. The UV–vis spectra were recorded using a UV 1901 spectroscopy. The pH of solution was measured using a Mettler Toledo S20K pH meter.

Synthesis of TTU-SBA-15 and TT-SBA-15

The detailed procedures for the synthesis and the structural characterization of Tpu-SBA-15 [36] and APTES-SBA-15 [32] have been reported in our previous work. The preparation details of TTU-SBA-15 are shown in Scheme S1 as follows: briefly, Tpu-SBA-15 (0.5 g) and TT (0.2764 g, 1 mmol) were dispersed in 30 mL anhydrous ethyl alcohol (EtOH); the reaction mixture was stirred at 80 °C for 24 h. After cooling to ambient temperature, TTU-SBA-15 was separated by centrifugation, washed with chloroform to remove unreacted TT, and then dried at 80 °C for 12 h. According to the TGA data (Fig. S1a), the amount of functional group in SBA-15 was approximately 0.54 mmol g^{-1}.

The synthetic procedure of TT-SBA-15 was similar to that of TTU-SBA-15, while Tpu-SBA-15 was changed to APTES-SBA-15 (Scheme S1). The TGA curves of TT-SBA-15 indicated an obvious weight loss (Fig. S1b); the amount of functional group in SBA-15 was approximately 0.80 mmol g^{-1}.

Fluorescence measurements

In a typical detection experiment, 10 mg of TTU-SBA-15 (or TT-SBA-15) was sonicated in 20 mL of HEPES buffer (20 mM, pH = 7) for about 15 min, and a stable suspension solution of TTU-SBA-15 or TT-SBA-15 (0.5 g L^{-1}) was obtained. Then, the 4.5 mL of each analyte with required concentration was added into 0.5 mL TTU-SBA-15 (or TT-SBA-15) suspension solution, such as MB, MLB, MG,

litmus, Azure A, Azure B, Na^+, K^+, Mg^{2+}, Ca^{2+}, Ba^{2+}, Ni^{2+}, Cu^{2+}, Zn^{2+}, Cd^{2+}, Hg^{2+}, Al^{3+}, and Co^{2+}. All the mixed suspensions stood at room temperature for 12 h before fluorescence measurements. For the concentration studies, TTU-SBA-15 (0.5 g L^{-1}) was diluted to the required concentrations in the range of 0.025–0.50 g L^{-1}. For the time and temperature studies, the fluorescence spectra of TTU-SBA-15 (0.05 g L^{-1}) was tested over 6–72 h at 30–80 °C. Unless stated, all of the experiments were carried out in in aqueous solution (20 mM HEPES buffer, pH = 7.0). All fluorescence measurements were repeated three times, and the results were reproducible.

For the competition studies, 0.5 mL of TTU-SBA-15 (0.5 g L^{-1}) and 2.5 mL MO (2.0×10^{-4} M) along with 2.0 mL other interfering dyes (7.5×10^{-4} M) were mixed. All fluorescence measurements were repeated three times, and then the relative intensity I/I_0 was calculated, where I_0 was the fluorescence intensity of TTU-SBA-15 and I was the fluorescence intensity of TTU-SBA-15 in the presence of the dyes. For real samples test, the deionized water was changed to tap water. For pH studies, hydrochloric acid and sodium hydroxide were employed to adjust pH values.

Adsorption experiments

About 20 mg of TTU-SBA-15 was mixed with 20 mL MO solutions of different concentrations (i.e., 5, 10, 15, 20, and 30 mg L^{-1}). The suspensions were then stirred for 12 h at room temperature to achieve equilibrium. After centrifugation, the UV absorption of the supernatant was measured, and the MO concentration remaining in the solution after adsorption was calculated according to the standard curve of MO (Fig. S2). The equilibrium adsorption capacity is then evaluated according to the equation: $q_e = (C_0 - C_e)V/m$, where q_e is the equilibrium adsorption capacity (mg/g), C_0 and C_e are the initial and final concentration of MO in an aqueous solution (mg/L), V is the volume of the solution (L), and m is the weight of the material (g). The data are fitted with the Langmuir model ($C_e/q_e = C_e/q_{max} + q_{max} \bullet k_L$), where q_e (mg/g) and q_{max} (mg/g) are the equilibrium adsorption capacity and the maximum adsorption capacity, respectively, C_e (mg L^{-1}) is the equilibrium MO concentrations, and K_L (L/mg) is the Langmuir adsorption constant.

Reproducibility study

About 40 mg of TTU-SBA-15 was treated with 40 mL of water and MO (1.0×10^{-5} M) solution, respectively. After stirring for 1 h at room temperature, the fluorescent spectra were measured. The used TTU-SBA-15 was centrifuged, cleaned several times with 50 °C deionized water, dried at 100 °C for 8 h, and then used again for the determination of MO. These processes were repeated three times.

Limit of detection (LOD) and quenching constant (K_{SV}) calculations

The LOD is calculated according to the equation $LOD = 3\sigma/k$, where σ is standard deviation of blank solutions of TTU-SBA-15 measured by ten times and k is the slope of fluorescence intensity at 452 nm versus [MO]. An exponential quenching equation $F_0/F = K_{SV}[m] + 1$ is used to fit the Stern–Volmer curve and calculate the quenching constant (K_{SV}) of TTU-SBA-15 toward MO. In this equation, F_0 and F are the fluorescence intensity of the TTU-SBA-15 at 452 nm, in the absence and presence of MO, and [m] is the concentration of MO.

Theoretical calculations

Theoretical calculations of quantum chemical optimization on the energy levels of MO and organic functions of TTU-SBA-15 were performed, based on the density functional theory (DFT) method at the B3LYP/6-31G(d) level using a Gaussian 09 program.

Results and discussion

TT-SBA-15 and TTU-SBA-15 were prepared by grafting TT to the amine- and urea-functionalized mesoporous SBA-15 silica, respectively. The preparation protocols of the materials TT-SBA-15 and TTU-SBA-15 are shown in Scheme S1, and the detailed procedures are provided in the "Experimental" section. The chemical structures and their corresponding solid-state images of TT, TT-SBA-15, and TTU-SBA-15 are shown in Fig. 1. In the solid state, TT, TT-SBA-15, and TTU-SBA-15 showed orange yellow, yellow, and light yellow color under daylight and bright yellow, yellow, and green color when exposed to 365 nm UV light, respectively (Fig. 1).

Characterization of TTU-SBA-15 and TT-SBA-15

The successful grafting of organic functional groups and preservation of the mesoporous structure of the sensor materials were investigated via SXRD, TEM, TGA, FT-IR, and N_2 adsorption–desorption experiments. The SXRD patterns of TTU-SBA-15 and TT-SBA-15 are shown in Fig. 2a and S3a, respectively. The three well-resolved broad Bragg reflections observed in these patterns could be assigned to the (100), (110), and (200) planes, which was similar to the hexagonal structure of SBA-15 [26]. The TEM images displayed the ordered parallel channels of TTU-SBA-15 (Fig. 2b) and TT-SBA-15 (Fig. S3b). These findings indicated that the functionalized mesoporous materials retain the uniform pore structure of SBA-15.

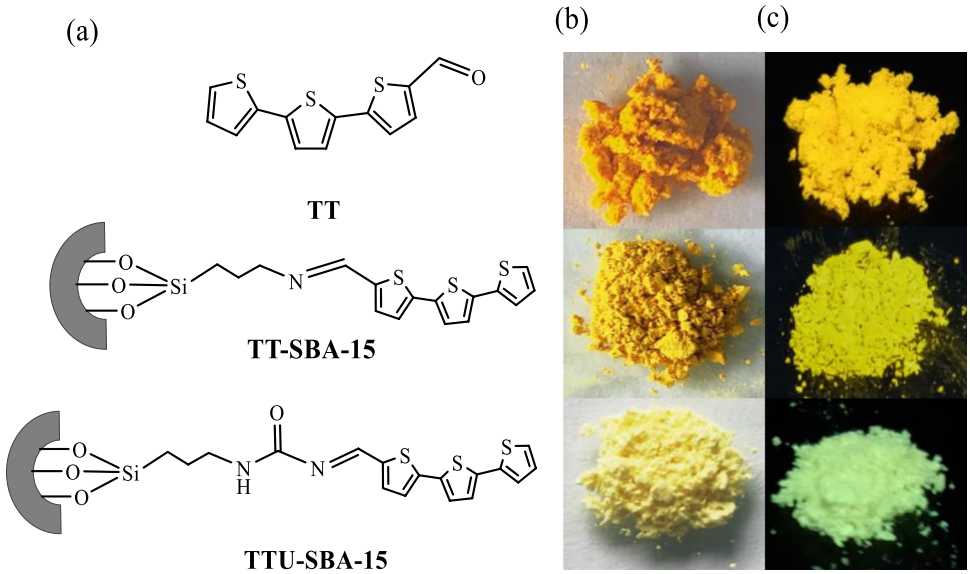

Fig. 1 Chemical structures (**a**) and solid-state photographs of TT, TT-SBA-15, and TTU-SBA-15 under day light (**b**) and 365 nm UV light irradiation (**c**)

Figure 2c showed the N_2 adsorption–desorption isotherms of the mesoporous silica materials. TTU-SBA-15 and TT-SBA-15 displayed the same type IV isotherms as SBA-15, with obvious H1-type hysteresis loops, thus reflecting the capillary condensation of N_2 in a large uniform cylindrical mesoporous material [37]. Compared with those of SBA-15, the BET surface areas, pore diameters and pore volumes of TTU-SBA-15 and TT-SBA-15 were smaller (Table S1), which indicated the successful introduction of organic groups to the interior of the SBA-15 channels [38].

The FT-IR spectra of pure SBA-15, Tpu-SBA-15, and TTU-SBA-15 were displayed in Fig. 2d. All of the obtained spectra showed the broad O – H stretching band of Si – OH groups at approximately 3442 cm^{-1} and the characteristic bands of Si – O – Si bands at 462, 802, and 1081 cm^{-1}, thus confirming the existence of the SBA-15 silica framework. Two new peaks at 2922 and 2850 cm^{-1} could be observed in the FT-IR spectrum of TTU-SBA-15, and these bands were attributed to the stretching vibration of C – H. New peaks at 1650 and 1558 cm^{-1} corresponded to the stretching vibrations of C = O and N – H [39], respectively, and the peaks at 1456 and 1343 cm^{-1} could be attributed to the stretching vibrations of C = C in the thiophene ring. Another peak appearing at 694 cm^{-1} could be attributed to the stretching vibrations of C – S in the thiophene ring. Figure S4 showed the FT-IR spectra of SBA-15, APTES-SBA-15, and TT-SBA-15. Similar to the previous samples, all of the obtained FT-IR spectra showed the broad O – H stretching band of Si – OH groups at approximately 3436 cm^{-1} and the characteristic bands of Si – O – Si at 462, 802, and 1081 cm^{-1}. Compared with that of SBA-15, the FT-IR spectrum of APTES-SBA-15 showed two new peaks at 2926 and 2864 cm^{-1}, which corresponded to C – H stretching vibrations. New peak at 1550 cm^{-1} was attributed to the N – H stretching vibrations. After grafting of the terthiophene group, the peak at 1550 cm^{-1} disappeared, and two new peaks appeared at 1461 and 872 cm^{-1}; these peaks were attributed to the stretching vibrations of C = C and C – S in the thiophene ring [39]. Thus, the FT-IR spectra confirmed the retention of the mesoporous material structure of SBA-15 as well as the incorporation of TT into the SBA-15 framework.

Optimization of detection conditions

The normalization fluorescence emission and excitation spectra of TTU-SBA-15 in an aqueous solution (Fig. S5) displayed an emission band centered at 452 nm at the optimum excitation of 368 nm.

In order to apply TTU-SBA-15 as a fluorescence sensor, the suitable detection conditions, such as concentration, time, temperature, and pH, were investigated firstly. Upon increasing the concentrations (0.025–0.50 g L^{-1}) of TTU-SBA-15, the fluorescence intensity of TTU-SBA-15 at 452 nm increased gradually (Fig. S6a). Then, the concentration of 0.05 g L^{-1}, which is within the linear range (Fig. S6b), was selected for studying on other conditions. The fluorescence or the fluorescence intensity of TTU-SBA-15 at 452 nm was stable over the time of 12–72 h (Fig. S7), the temperature of 30–80 °C (Fig. S7), and the pH range of 6.0–12.0 (Fig. S8). Unless otherwise stated, the detection conditions of TTU-SBA-15 were selected as concentration of 0.05 g L^{-1}, time of 12 h, temperature of 30 °C, and pH of 7.0 in the subsequent experiments.

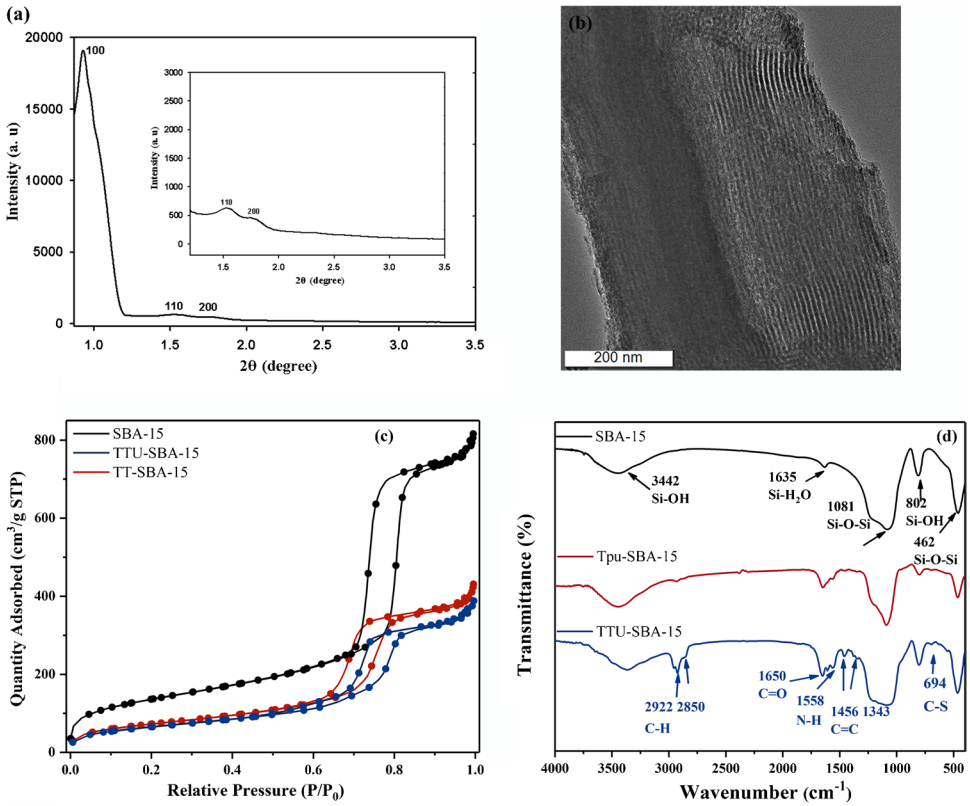

Fig. 2 **a** SXRD pattern and **b** TEM image of TTU-SBA-15. **c** N_2 adsorption–desorption isotherms of SBA-15, TTU-SBA-15 and TT-SBA-15 and **d** FT-IR spectra of SBA-15, Tpu-SBA-15, and TTU-SBA-15

Sensitivity of TTU-SBA-15 toward MO

The fluorescence response of TTU-SBA-15 to MO is illustrated in Fig. 3. TTU-SBA-15 had a "switch-off" response to MO at 452 nm, and the fluorescence intensity of the TTU-SBA-15 gradually decreased with increasing MO concentration (0 – 0.1 mM) (Fig. S9). The color of the solution clearly changed from blue to black under 365 nm excitation (inset Fig. 3). Good linearity between the detected fluorescence intensity and MO concentration could be observed at the low concentration range of 0.20 – 2.0 μM with a high squared correlation coefficient of 0.99 (Fig. 4a). According to the equation LOD $= 3\sigma/k$, the theoretical detection limit of TTU-SBA-15 could be evaluated from the fluorescence titration curve to be 0.092 μM. As shown in the Stern–Volmer curve (Fig. 4b), the fluorescence response of TTU-SBA-15 at 452 nm under the presence of different MO concentrations solutions was linear in the low concentration range of 0.20 – 2.0 μM. At higher MO concentrations, the curve deviated from linearity, and the slope increased gradually. This phenomenon was likely because of self-adsorption process [40] (discussed later). The quenching constant (K_{SV}) of TTU-SBA-15 for MO is calculated to be $8.50 \times 10^4\ M^{-1}$ (Fig. 4b). By comparison, the fluorescence emission of TT-SBA-15 at 454 nm was gradually quenched in the presence of MO (Fig. S10 and S11), and the K_{SV} of TT-SBA-15 for MO was calculated to be $4.80 \times 10^4\ M^{-1}$ (Fig. S12). Compared with TT-SBA-15, TTU-SBA-15 had a higher quenching constant, which indicates that it had better sensing performance for MO.

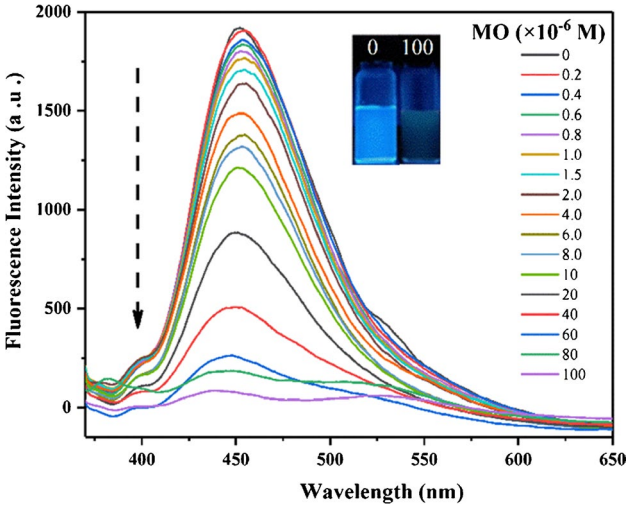

Fig. 3 The fluorescence spectra of TTU-SBA-15 (0.05 g L^{-1}) in the presence of different concentrations of MO in aqueous solution (20 mM HEPES buffer, pH = 7.0) (inset: the photographs under a 365 nm UV lamp) (λ_{ex} = 368 nm, λ_{em} = 452 nm)

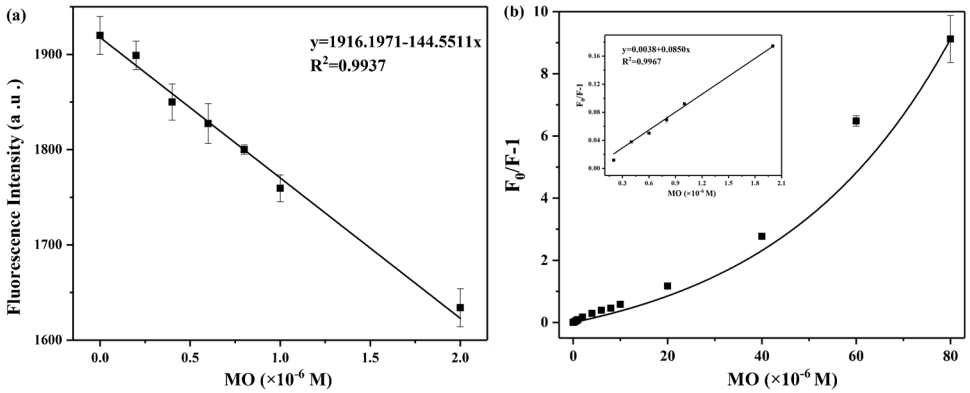

Fig. 4 **a** Fluorescence intensity of TTU-SBA-15 (0.05 g L^{-1}) at 452 nm versus the concentration of MO. **b** The Stern–Volmer plot for MO. Inset: Linear range of the Stern–Volmer plot (the error bars represent the standard deviation of three measurements)

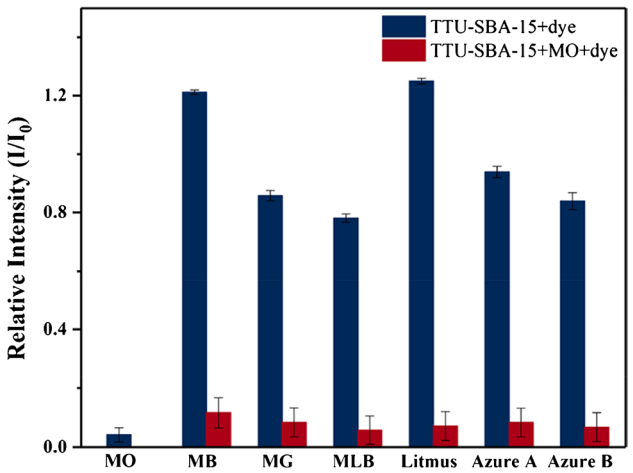

Fig. 5 The relative intensity (I/I_0) of TTU-SBA-15 (0.05 g L^{-1}) in the presence of dyes in aqueous solution (20 mM HEPES buffer, pH = 7.0). Blue bars: each dye (1.0×10^{-4} M) was added. Red bars: MO (1.0×10^{-4} M) and each of the other dyes (3.0×10^{-4} M) were added (the error bars represent the standard deviation of three measurements)

Selectivity of TTU-SBA-15 toward MO

Considering that MO is an anionic dye, seven organic dyes with different charges, namely, negatively charged MO and MB, positively charged MG, MLB, Azure A and Azure B, and litmus, were selected to evaluate the ability of TTU-SBA-15 to detect MO selectively. As shown in Fig. 5 and S13, the peak at 452 nm was dramatically quenched after addition of MO to the suspension of TTU-SBA-15. Moreover, the fluorescence of TTU-SBA-15 showed minimal variations upon addition of all other dyes, which means that electrostatic interaction was not the main force driving fluorescence quenching. Furthermore, TTU-SBA-15 could effectively detect MO among the mixture of MO and other dyes (Fig. 5), demonstrating the excellent selectivity and anti-interference capability of TTU-SBA-15 towards MO. By comparison, the fluorescence of TT-SBA-15 revealed obvious quenching after addition of both MO and MB (Fig. S14), thus demonstrating that TTU-SBA-15 had better selectivity for MO than TT-SBA-15.

Actual water samples may contain various metal ions. To investigate the effect of metal ions on the detection of MO, we conducted an experiment including different metal ions and found that the presence of metal ions has no influence on the fluorescence of TTU-SBA-15 (Fig. S15). However, TT-SBA-15 responded to some metal ions (Fig. S16), which means that these ions could interfere with the detection of MO in real samples when TT-SBA-15 was used. These results demonstrated that the functional groups in the optical receptor could affect metal-ion selectivity of the sensor. According to the above analysis, TTU-SBA-15 could selectively recognize MO in the presence of various dyes and metal ions.

The reusability of nanomaterials is an important factor for its economic efficiency. Thus, the recovery experiments were performed to evaluate the reproducibility characteristic of TTU-SBA-15. As shown in Fig. S17, by comparing the fluorescence spectra of fresh TTU-SBA-15 and the regenerated TTU-SBA-15 after using for MO detection, it can be found that the fluorescence intensity of TTU-SBA-15 at 452 nm maintained 95.5%, 92.4%, and 87.4%, respectively, after the first, second, and third cycle of detecting MO. Therefore, TTU-SBA-15 showed good recoverability, thus highlighting the potential use of the proposed sensor in practical applications.

The performance of TTU-SBA-15 toward MO had been compared with those nanomaterials based on different detection methods. As was evident from Table S3, compared to most of the reported materials, TTU-SBA-15 displayed several promising properties: (1) fluorescence detection didn't require expensive equipments, which is simple to operate and responds quickly; (2) compared with other fluorescence sensors, TTU-SBA-15 had excellent selectivity and anti-interference ability for MO detection; and (3) TTU-SBA-15 and other fluorescence sensors had comparable detection limits.

Possible sensing mechanism

The effects of pH on the detection performance of TTU-SBA-15 toward MO were evaluated (Fig. S8). The fluorescence intensity of TTU-SBA-15 at 452 nm showed slight variations over the pH range of 3.0 – 14.0, while almost no fluorescence intensity changes at 452 nm were observed in the presence of MO over the tested pH range. Such a wide pH detection range demonstrated the adaptability of TTU-SBA-15 to different pH environments as well as its suitability for practical applications. Moreover, these findings implied that electrostatic and hydrogen bonding interactions were not the driving forces for the sensing. Thus, the π-π interactions between TTU-SBA-15 and MO may be the main factors influencing the fluorescence quenching.

In order to explain the fluorescence quenching of TTU-SBA-15 by MO, the energy levels of the highest occupied molecular orbital (HOMO) and the lowest unoccupied molecular orbital (LUMO) of MO and the organic units of TTU-SBA-15 were investigated. As shown in Fig. 6, the LUMO energy level of the organic functions is lower than that of MO, indicating that the electron transfer process did not involve in the fluorescent response [16]. Next, we compared the overlaps between the UV–vis spectra of various dyes and the emission spectra of TTU-SBA-15. It was obvious that the absorption range of MO (350 – 550 nm) significantly overlapped with the emission range of TTU-SBA-15 (380 – 600 nm), while slight or almost no overlap was observed for the other investigated dyes (Fig. S18). Thus, the quenching mechanism for detecting MO could be the fluorescence resonance energy transfer (FRET) or inner filter effect (IFE) [41].

To further explore the quenching mechanism, the related fluorescence lifetimes were measured. As shown in Table S2, the average fluorescence lifetimes of TTU-SBA-15 in the absence and presence of MO were 1.72 ns and 3.48 ns, respectively. The significant difference between the fluorescence lifetimes of TTU-SBA-15 and TTU-SBA-15-MO and the upward Stern–Volmer plot (Fig. 4b) demonstrates that the fluorescence quenching was caused by both static and dynamic pathway [41]. The increased fluorescence lifetime may be attributed to the MO-induced aggregation of the terthiophene fluorophore in the confined mesopores of TTU-SBA-15 [42], which involved the adsorption process of MO onto TTU-SBA-15, and the appearance of a new shoulder emission peak at 510 nm also confirmed the aggregates (Fig. 3 and S19).

To confirm the above assumptions, the adsorption capacity of TTU-SBA-15 toward MO was examined. Langmuir model could better describe the adsorption of MO onto TTU-SBA-15 (Fig. S20), indicating that adsorption occurs through monolayer physical adsorption, i.e., MO is adsorbed on the surface of the material. The adsorption process facilitates the diffusion of MO into the mesoporous TTU-SBA-15, thereby increasing the contact probability between the organic functions of TTU-SBA-15 and MO through the π-π interactions [43]. The effective interactions shortened the distances of the organic functions as well as the distances between the organic functions and MO, which induced the aggregation and improved the chance of FRET, leading to the increased fluorescence lifetime and improved detection sensitivity. Therefore, the quenching mechanism was mainly due to FRET rather than IFE, and the possible detection mechanism of TTU-SBA-15 for trace MO is shown in Scheme 1.

Detection of MO in real water samples

MO detection was carried out in a tap water sample to demonstrate the feasibility of TTU-SBA-15 in practical applications. A standard working plot was used to detect the MO concentration in the sample, and the results are shown in Table 1. The MO concentration determined was consistent with the amount added, and the quantitative recoveries of MO were between 98.3 and 103.0%. These results indicate that the proposed strategy could simply and accurately detect trace MO concentrations in real water samples.

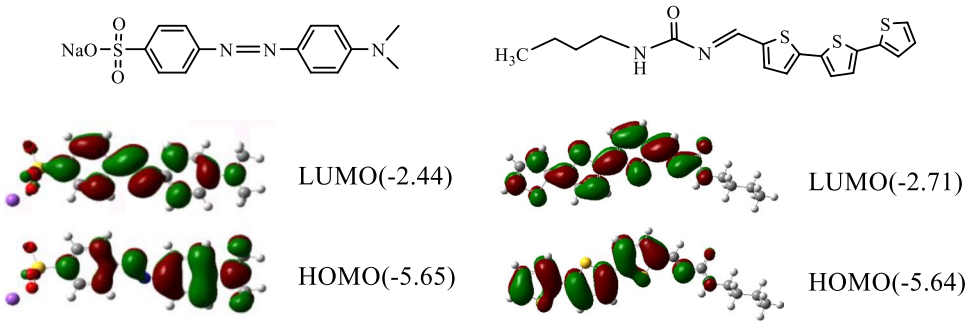

Fig. 6 Calculated molecular orbital energy levels of MO and organic functions on TTU-SBA-15 based on B3LYP/6-31G basis set

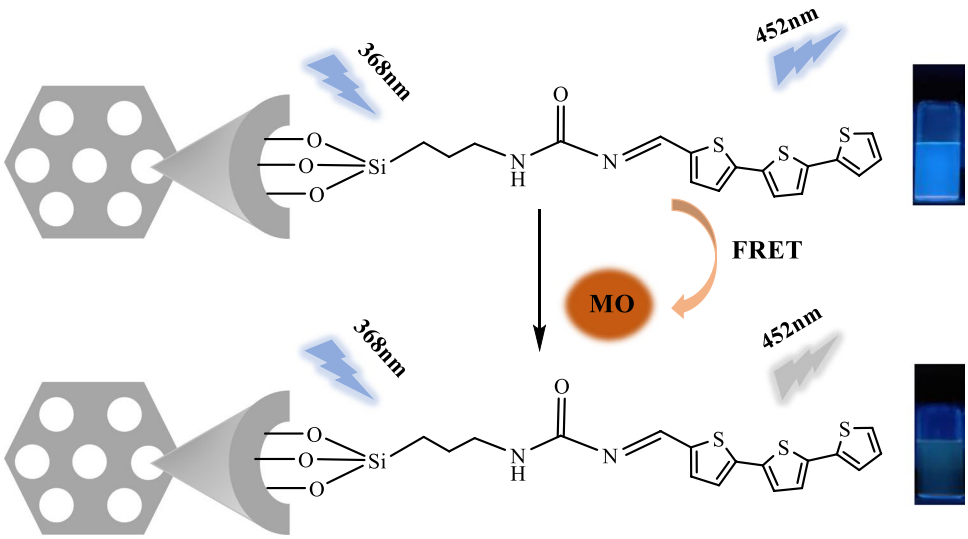

Scheme 1 Proposed mechanism for the detection of MO

Table 1 Determination of MO in real water samples ($n = 3$)

Source of samples	MO added/ μM	MO found/ μM	Recovery/%	RSD/%
Tap water	2.0	2.06 ± 0.05	103.0 ± 2.5	0.046
	4.0	4.09 ± 0.08	102.2 ± 2.0	0.12
	8.0	7.86 ± 0.13	98.3 ± 1.6	0.15

Conclusion

We prepared an organic–inorganic hybrid mesoporous material, i.e., TTU-SBA-15, and demonstrated its applicability as a fluorescence sensor for detecting MO with high selectivity and sensitivity. TTU-SBA-15 showed obvious fluorescence quenching upon exposure to MO at approximately 452 nm in aqueous media in line with the FRET mechanism. When exposed to other dyes and metal ions, TTU-SBA-15 exhibited very slight fluorescent quenching. TTU-SBA-15 demonstrated high sensitivity, excellent selectivity, a very low detection limit, wide pH range, and good recovery performance, thus indicating that TTU-SBA-15 can be used in different environments for detecting MO. Based on the above sensing capacity, TTU-SBA-15 is suggested as a potential fluorescence sensor for MO. This research offers an effective strategy for the identification of dye type and concentration prior to treatment and degradation. The proposed method provides an idea for the detection of analytes by combining mesoporous silica materials with different organic functional groups.

Supplementary Information The online version contains supplementary material available at https://doi.org/10.1007/s00604-021-05063-x.

Funding This work was supported by the National Natural Science Foundation of China (NSFC) (Grant Nos. 21966006) and Natural Science Foundation of Guangxi Province (Grant No. 2018GXNSFAA050015).

Declarations

Conflict of interest The authors declare no competing interests.

References

1. Abdi J, Vossoughi M, Mahmoodi NM, Alemzadeh I (2017) Synthesis of amine-modified zeolitic imidazolate framework-8, ultrasound-assisted dye removal and modeling. Ultrason Sonochem 39:550–564
2. Li X, Wang Y, Zhang P, Ge W (2021) Highly sensitivity, selectivity chemosensor for methyl orange using upconversion NaBiF4: Yb/Tm nanosheets. J Solid State Chem 301:12230
3. Sun HM, Ju CG, Zhao YW, Wang CY, Wu Y (2020) Preparation of SiO_2@ZIF-67/CNTs and research on its adsorption performance at low-temperature. Colloid Surface A 603:125205
4. Derami HG, Gupta P, Gupta R, Rathi P, Morrissey JJ, Singamaneni S (2020) Palladium nanoparticle-decorated mesoporous polydopamine/bacterial nanocellulose as a catalytically active universal dye removal ultrafiltration membrane. ACS Appl Nano Mater 3:5437–5448
5. Sena S, Demirer GN (2003) Anaerobic treatment of real textile wastewater with a fluidized bed reactor. Water Res 37:1868–1878
6. Hassanzadeh-Tabrizi SA, Motlagh MM, Salahshour S (2016) Synthesis of ZnO/CuO nanocomposite immobilized on c-Al_2O_3 and application for removal of methyl orange. Appl Surf Sci 384:237–243
7. Ranjith KS, Manivel P, Rajendrakumar RT, Uyar T (2017) Multifunctional ZnO nanorod-reduced graphene oxide hybrids nanocomposites for effective water remediation: effective sunlight driven degradation of organic dyes and rapid heavy metal adsorption. Chem Eng J 325:588–600
8. Parmar B, Bisht KK, Rajput G, Suresh E (2021) Recent advances in metal–organic frameworks as adsorbent materials for hazardous dye molecules. Dalton Trans 50:3083–3108

9. Shan Z, Lu MS, Curry DE, Beale S (2017) Regenerative nanobots based on magnetic layered double hydroxide for azo dye removal and degradation. Chem Commun 53:10456–10458
10. Meng S, Yu S, Tang F, Hu X, Lu J, Fei X, Zhu M (2021) Fiber engineering of silica-based aerogels with surface specificity and regenerability for continuous removal of dye pollutants from wastewaters. Microporous Mesoporous Mater 314:110874
11. Majee BP, Srivastava V, Mishra AK (2020) Surface-enhanced Raman scattering detection based on an interconnected network of vertically oriented semiconducting few-layer MoS_2 Nanosheets. ACS Appl Nano Mater 3(5):4851–4858
12. Nguyen TV, Vu DC, Pham VH, Bui H (2021) Improvement of SERS for detection of ultra-low concentration of methyl orange by nanostructured silicon decorated with Ag nanoparticles. Optik 231:166431
13. Fang GZ, Wu Y, Dong XM (2013) Simultaneous determination of banned acid orange dyes and basic orange dyes in foodstuffs by liquid chromatography-tandem electrospray ionization mass spectrometry via negative/positive ion switching mode. J Agric Food Chem 61:3834–3841
14. Witkowski B, Ganeczko M, Biesaga M (2017) Identification of orcein and selected natural dyes in 14th and 15th century liturgical paraments with high-performance liquid chromatography coupled to the electrospray ionization tandem mass spectrometry (HPLC-ESI/MS/MS). Microchem J 133:370–379
15. Tropp J, Ihde MH, Azoulay JD (2020) A sensor array for the nanomolar detection of azo dyes in water. ACS Sen 5:1541–1547
16. Liu TH, Ding LP, Zhao KR (2012) Single-layer assembly of pyrene end-capped terthiophene and its sensing performances to nitroaromatic explosives. J Mater Chem 22:1069–1077
17. Wu M, Sun LJ, Miao KS, Wu YZ, Fan LJ (2018) Detection of Sudan dyes based on inner-filter effect with reusable conjugated polymer fibrous membranes. ACS Appl Mater Interfaces 10:8287–8295
18. Wang J, Liu HB, Tong Z, Ha CS (2015) Fluorescent/luminescent detection of natural amino acids by organometallic systems. Coord Chem Rev 303:139–184
19. Hu Y, Gao Z (2020) Sensitive detection of Sudan dyes using tire-derived carbon dots as a fluorescent sensor. Spectrochim Acta A Mol Biomol Spectrosc 239:118514
20. Fang AJ, Long Q, Zhang Y (2016) Upconversion nanosensor for sensitive fluorescence detection of Sudan I-IV based on inner filter effect. Talanta 148:129–134
21. Ye XL, Zhang J, Chen H, Huang F (2014) Fluorescent nanomicelles for selective detection of Sudan dye in Pluronic F127 aqueous media. ACS Appl Mater Interfaces 6(7):5113–5121
22. Bogireddy NKR, Lara J, Fragoso LR, Agarwal V (2020) One-step hydrothermal preparation of highly stable N doped oxidized carbon dots for toxic organic pollutants sensing and bioimaging. Chem Eng J 401:126097
23. Zhao DY, Feng JL, Huo QS (1998) Copolymer syntheses of mesoporous silica with periodic 50 to 300 angstrom pores. Science 279:548–552
24. Kim H, Rao BA, Jeong J, Angupillai S, Choi JS, Nam JO, Lee CS, Sona YA (2016) A rhodamine scaffold immobilized onto mesoporous silica as a fluorescent probe for the detection of Fe (III) and applications in bio-imaging and microfluidic chips. Sens Actuators B Chem 224:404–412
25. Paul L, Mukherjee S, Chatterjee S, Bhaumik A (2019) Organically functionalized mesoporous SBA-15 type material bearing fluorescent sites for selective detection of HgII from aqueous medium. ACS Omega 4:17857–17863
26. Liu HB, Liang YH, Liang J (2020) Pyrene derivative-functionalized mesoporous silica–Cu^{2+} hybrid ensemble for fluorescence "turn-on" detection of H_2S and logic gate application in aqueous media. Anal Bioanal Chem 412:905–913
27. Wan XJ, Yao S, Liu HY, Yao YW (2013) Selective fluorescence sensing of Hg^{2+} and Zn^{2+} ions through dual independent channels based on the site-specific functionalization of mesoporous silica nanoparticles. J Mater Chem A 1:10505–10512
28. Dong ZP, Tian X, Chen YZ, Hou JR, Ma JT (2013) Rhodamine group modified SBA-15 fluorescent sensor for highly selective detection of Hg^{2+} and its application as an INHIBIT logic device. RSC Adv 3:2227–2233
29. Zarabadi-Poor P, Badiei A, Yousefi AA, Barroso-Flores J (2013) Selective optical sensing of Hg (II) in aqueous media by H-acid/SBA-15: a combined experimental and theoretical study. J Phys Chem C 117:9281–9289
30. Gao M, Zeng J, Liang K, Zhao D, Kong B (2020) Interfacial assembly of mesoporous silica based optical heterostructures for sensing applications. Adv Funct Mater 30:1906950
31. Enshirah D (2017) Adsorption of heavy metals on functionalized-mesoporous silica: a review. Microporous Mesoporous Mater 247:145–157
32. Wang J, Zhang X, Liu HB, Zhang D, Nong H, Wu P, Chen P, Li D (2020) Aggregation induced emission active fluorescent sensor for the sensitive detection of Hg^{2+} based on organic–inorganic hybrid mesoporous material. Spectrochim Acta A Mol Biomol Spectrosc 227:117585
33. Zhao LY, Li JY, Sui D, Wang Y (2017) Highly selective fluorescence chemosensors based on functionalized SBA-15 for detection of Ag^{+} in aqueous media. Sens Actuators B Chem 242:1043–1049
34. Pal P, Rastogi SK, Gibson CM, Aston DE, Branen AL, Bitterwolf TE (2011) Fluorescence sensing of zinc(II) using ordered mesoporous silica material (MCM-41) functionalized with N-(quinolin-8-yl)-2-[3-(triethoxysilyl)pro-pylamino]acetamide. ACS Appl Mater Interfaces 3:279–286
35. Gao ZP, Qiao M, Tan MM, Peng HN, Ding LP (2020) Surface functionalization of mesoporous silica nanoparticles with pyronine derivative for selective detection of hydrogen sulfide in aqueous solution. Colloids Surf A 586:124194
36. Huang J, Liu HB, Wang J (2021) Functionalized mesoporous silica as a fluorescence sensor for selective detection of Hg^{2+} in aqueous medium. Spectrochim Acta A Mol Biomol Spectrosc 246:118974
37. Lashgaria N, Badieia A, Ziarani GM (2017) A novel functionalized nanoporous SBA-15 as a selective fluorescent sensor for the detection of multianalytes (Fe^{3+} and $Cr_2O_7^{2-}$) in water. J Phys Chem Solids 103:238–248
38. Wu HM, Xiao Y, Guo Y (2020) Functionalization of SBA-15 mesoporous materials with 2-acetylthiophene for adsorption of Cr(III) ions. Microporous Mesoporous Mater 292:109754
39. Timin AS, Rumyantsev EV, Solomonov AV, Musabirov II, Sergeev SN, Ivanov SP, Berlier G, Balantseva E (2015) Preparation and characterization of organo-functionalized silicas for bilirubin removal. Colloids and Surfaces A: Physicochem Eng Aspects 464:65–77
40. Wang C, Li QL, Wang B (2018) Fluorescent sensors based on AIE-genfunctionalised mesoporous silica nanoparticles for the detection of explosives and antibiotics. Inorg Chem Front 5:2183
41. Ma C, Li P, Xia L, Qu F, Kong RM, Song ZL (2021) A novel ratiometric fluorescence nanoprobe for sensitive determination of uric acid based on CD@ZIF-CuNC nanocomposites. Microchim Acta 188:259
42. Pyo K, Thanthirige VD, Kwak K, Pandurangan P, Ramakrishna G, Lee D (2015) Ultrabright luminescence from gold nanoclusters: rigidifying the Au(I)-thiolate shell. J Am Chem Soc 137(25):8244–8250
43. Wang J, Ma Q, Wang Y, Li Z, Li Z, Yuan Q (2018) New insights into the structure–performance relationships of mesoporous materials in analytical science. Chem Soc Rev 47:8766–8803